Promotion effects of alkali metals on iron molybdate catalysts for CO2 catalytic hydrogenation

Yong Zhou, Aliou Sadia Traore, Deizi Peron, Alan Barrios, Sergei Chernyak, Massimo Corda, Olga Safonova, Achim Iulian Dugulan, Ovidiu Ersen, Mirella Virginie, et al.

Promotion effects of alkali metals on iron molybdate catalysts for the catalytic hydrogenation of CO_2 to light olefins

Yong Zhou [a], Sergei A. Chernyak [a], Massimo Corda [a], Olga V. Safonova [b], Achim Iulian Dugulan [c], Aliou Sadia Traore [d], Ovidiu Ersen [d], Deizi V. Peron [a], Alan J. Barrios [a], Vitaly V. Ordomsky [a] and Andrei Y. Khodakov [a]**

[a]*University of Lille, CNRS, Centrale Lille, University of Artois, UMR 8181−UCCS−Unité de Catalyse et Chimie du Solide, Lille F-59000, France*

[b] *Paul Scherrer Institute, CH-5232 Villigen, Switzerland*

[c] *Fundamental Aspects of Materials and Energy Group, Delft University of Technology, Mekelweg 15, Delft 2629 JB, Netherlands*

[d] *IPCMS, UMR 7504 CNRS, Université de Strasbourg, 23 rue du Loess, BP 43, Cedex 2, 67034 Strasbourg, France*

Corresponding authors: Vitaly V. Ordomsky (vitaly.ordomsky@univ-lille.fr) , Andrei Y. Khodakov (andrei.khodakov@univ-lille.fr)

Abstract

CO_2 hydrogenation is an attractive way to store and to utilize carbon dioxide generated by industrial processes, as well as a method for producing valuable chemicals from a renewable and abundant resource. Iron catalysts are commonly used for the hydrogenation of carbon oxides to hydrocarbons. Iron-molybdenum catalysts have found numerous applications as catalysts. However, they have been never evaluated in the CO_2 hydrogenation.

In this work, iron-molybdenum catalysts without and with a promoting alkaline metal (Li, Na, K, Rb or Cs) were characterized using X-ray diffraction, hydrogen temperature-programmed reduction, CO_2 temperature-programmed desorption, *in-situ* ^{57}Fe Mossbauer spectroscopy and *operando* X-ray adsorption spectroscopy and evaluated in the CO_2 hydrogenation. Under the reaction conditions, the catalysts form iron (II) molybdate structure, with partial reduction of molybdenum and iron carbidisation. The rate of CO_2 conversion and product selectivity strongly depend on the promoting alkaline metals, which electronegativity was identified as descriptor of the catalytic performance. Higher CO_2 conversion rates were observed on promoters with higher electronegativity, while low electronegativity of alkaline metals favours higher light olefin selectivity.

Graphical abstract

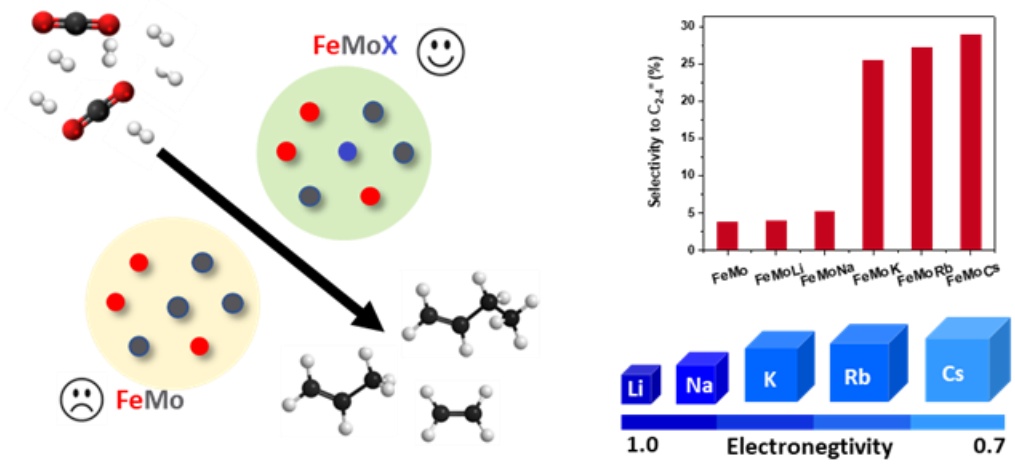

1. Introduction

The rising concentration of CO_2 in the atmosphere, a major greenhouse gas, is causing serious environmental problems such as global warming, ocean acidification, biodiversity crisis, etc[1-3]. This prompts us to take urgent action to stabilize the concentration of CO_2 in the atmosphere by reducing its emissions and developing effective technologies[4-6] to capture and to utilise CO_2.

To date, among the available tools, catalytic hydrogenation of CO_2 to value-added products, especially light olefins, with high activity, selectivity, and stability is highly desirable for various applications[7] and represents a practical way to achieve carbon neutrality. [8, 9] Along with much literature on optimized catalysts for Fischer-Tropsch synthesis (FTS), [10-13] iron- and cobalt-based catalysts are being tested for CO_2 hydrogenation. Compared to iron, cobalt catalysts preferably form methane in CO_2 hydrogenation[14, 15]. To maximize the production of light olefins, more attention has to be paid to the optimization of catalyst composition and structure. In our recent work[16], we identified the most efficient promoters and elucidated structure-performance correlations in the CO_2 hydrogenation to light olefins over zirconia-supported iron catalysts. The strongest promoting effect has been observed on iron catalysts containing alkaline metals and more particularly, potassium. A further increase in the light olefin selectivity could be realized by simultaneous promotion of iron catalysts with alkaline metals and molybdenum [16].

The promotion with alkali metals varies as a function of catalytic support. The electronic interaction of iron species and alkali may modify the intrinsic reaction rate

and selectivity. Alkali ions could enhance[3,4] carbon monoxide dissociation, because of election-donation effect on the iron species from basic oxygen species. The promotion by alkali metals reduces hydrogenation catalyst activity and increases the olefin to paraffin ratio in the reaction products. The WGS activity usually increases in the alkaline-promoted catalysts. The chain growth probability and selectivity to C_{5+} hydrocarbons are much higher over alkaline-promoted iron catalysts.

Iron molybdates with a tuneable Mo/Fe ratio are known for their high activity and stability, making them a popular choice for numerous catalytic applications. Some of the common reactions include oxidation of benzene, water gas shift reaction,[17] selective oxidation of methanol to formaldehyde,[18, 19] hydrogenation of alkenes, and dehydrogenation of alcohols. Iron molybdates can also play a role of precursors for obtaining highly dispersed iron species after activation. However, to the best of our knowledge, iron molybdates have never been used as catalysts for CO_2 hydrogenation. The structure of iron catalysts often evolves during catalytic reactions[20, 21], where different transformations of active phases are discovered[22, 23]. Therefore, in order to clarify the active sites and to improve the catalytic performances, it is critical to understand the structure and structural dynamics of the catalyst under the reaction conditions. *In-situ* characterizations of catalysts are promising strategies for identifying the instantaneous structure and understanding the structure-property relationship of catalysts[24-27]. *In-situ* characterizations under industrially relevant reaction conditions generally represents a significant experimental challenge, because of the typically used

high temperature, high pressure conditions and the presence of large number of reaction products etc.[20-22, 28]

In this paper, we prepared a series of iron-molybdenum catalysts and evaluated the effects of alkaline metals (Li, Na, K, Rb or Cs) on tuning the physicochemical properties and CO_2 hydrogenation performances of iron molybdate catalysts. To reveal the structure-performance correlations, iron molybdates promoted with alkali metals were characterized using several methods (X-ray diffraction, temperature-programmed reduction and desorption, high resolution transmission electron microscopy). In particular, the catalyst phase and structure evolution during activation and reaction were explored by *in-situ* Mössbauer spectroscopy and *operando* X-ray absorption spectroscopy (XAS). The reaction rate and selectivity were strongly affected by the alkaline promoters. A higher CO_2 reaction rate was favoured on catalysts with high-electronegative alkaline promoters, whereas higher light olefin selectivity was observed with low-electronegative promoters.

2. Experimental

2.1. Catalyst preparation

Iron (III) nitrate nonahydrate ($Fe(NO_3)_3 \cdot 9H_2O$, 99.99%), ammonium molybdate tetrahydrate ($(NH_4)_6Mo_7O_{24} \cdot 4H_2O$, 99.98%), lithium nitrate ($LiNO_3$, 99.99%), sodium nitrate ($NaNO_3$, 99.0%), potassium nitrate (KNO_3, 99.0%), rubidium nitrate ($RbNO_3$, 99.7%) and cesium nitrate ($CsNO_3$, 99.99%) were purchased from Sigma-Aldrich and used as precursors to prepare bulk FeMo-based catalysts. The catalysts were prepared

by adding a calculated amount of $Fe(NO_3)_3 \cdot 9H_2O$, $(NH_4)_6Mo_7O_{24} \cdot 4H_2O$ and eventually the respective alkali nitrate (~10% wt. Fe) in a mortal, and grinding them until reaching a homogeneous mixture. Then, they were calcined at 500 °C for 6 h under static air with a ramp of 2 °C/min. The obtained catalysts are denoted as FeMoX (X = Li, Na, K, Rb, or Cs).

2.2. Catalyst characterization

The catalyst chemical compositions were determined using an energy dispersive micro-X-ray fluorescence spectrometer-M4 TORNADO (Bruker). The sample was irradiated using a rhodium X-ray tube (50 kV/200 mA, 10 W). This X-ray source is equipped with a poly-capillary lens enabling excitation of an area of 200 μm. For each sample, 36 points (of 200 μm) were analysed covering the entire sample surface. The detector was a silicon-drift-detector Si(Li) with <145 eV resolution at 100 000 cps (Mn Kα) and cooled with Peltier cooling (−20 °C). The measurement was done under vacuum (20 mbar). Quantitative analysis was done using fundamental parameters (FP) (standardless). The quantification was made on the basis of the identified element. The catalyst crystal structure was characterized by X-ray powder diffraction (XRD) using a Bruker AXS D8 diffractometer with monochromatic Cu Kα radiation (λ = 0.1538 nm). The XRD patterns were collected with the 2θ range between 5-80°, using a step size of 0.02° and with an acquisition time of 0.5 s. The identification of crystalline phases present in the catalysts was carried out by comparison with the JCPDS standard software. The catalyst basicity was determined by CO_2 temperature-programmed

desorption (CO_2-TPD) on an AutoChem II 2920 apparatus (Micromeritics). Before the measurements, the samples were pre-treated at 500 °C in He for 1 h, cooled to 40 °C, and exposed to CO_2 for 30 min. The samples then were heated with a ramping rate of 10 °C/min to reach 700 °C in He flow. The CO_2 desorption was measured with a TCD detector. The reducibility of the catalysts was evaluated by hydrogen temperature-programmed reduction (H_2-TPR) using an AutoChem II 2920 apparatus (Micromeritics). The samples (~0.05 g) were reduced in a flow of 5% H_2/Ar flow (50 mL/min) and heated to 1000 °C with the temperature ramp rate of 10 °C/min. TEM and STEM analyses were carried using a TEM JEOL 2100F operating at 200 kV and equipped with a spherical aberrations corrector . STEM micrographs were acquired using a camera length of 12 cm and with a probe size of 0.1 nm. Elemental analyses were carried out with an energy dispersive X-ray spectroscopy (EDX) probe a silicon drift detector (SDD) with a sensor size of 60 mm^2 . The transmission ^{57}Fe Mössbauer spectra were collected at −153 °C with a sinusoidal velocity spectrometer using a ^{57}Co(Rh) source. The velocity calibration was carried out using an α-Fe foil at room temperature. The source and absorbing samples were kept at the same temperature during the measurements. The Mössbauer spectra were fitted using the Mosswinn 4.0 program[29]. The experiments were performed at pressures up to 10 bar, in a state-of-the-art high-pressure Mössbauer *in-situ* cell, which was recently developed at the Reactor Institute of Delft[30]. The high-pressure beryllium windows in this cell contained 0.08% Fe impurity, whose spectral contribution was fitted and removed from the final spectra. The *in-situ* X-ray absorption spectra were recorded at the Super XAS beamline station

of the Swiss Light Source (Villigen PSI, Switzerland). The beam was monochromatized by Si (111) crystal. Prior to the analysis, the catalyst diluted with carbon nanotube (weight ratio 1:1) was packed between two layers of quartz wool within a quartz capillary (O.D. = 2 mm). The measurements were performed under the flow of 5%CO/N_2 (P = 1 bar) for activation and $H_2/CO_2/N_2$ = 9/3/3, P = 6 bar) for the CO_2 hydrogenation at temperatures ranging from ambient to 350 °C. After the measurements, all data were processed by a ProQEXAFS software[31].

2.3. Catalytic performance tests

The catalytic performances in the CO_2 hydrogenation reaction were measured in a fixed-bed reactor with a 2 mm internal diameter and a length of 15 cm. The lower end of the reactor tube was filled with inert SiC (size of 500 μm), where ~110 mg of fresh catalyst had been loaded into the reactor. The catalysts were activated in CO under atmospheric pressure with a heating ramp of 2 °C/min until reaching the reaction temperature of 350 °C and dwelling at that temperature for 10 h under the CO flow (10 mL/min). After the activation, the catalysts were cooled to 180 °C, a gas mixture composed of H_2/CO_2 = 3 was fed into the reactor. Nitrogen with a flow of 1 ml/min was used as internal standard for the calculation of CO_2 conversion. After the flow rates and the pressure have been stabilized, the temperature was increased to 350 °C with a heating ramp of 2 °C/min to start the reaction. For the analysis of reactant and reaction products, a Varian CP-3800 chromatograph equipped with a TCD and an FID detector was used. Two columns were used: the first is a packed CTR-1 column connected to

the TCD detector, and the second is an Rt-Q-PLOT capillary column connected to the FID detector. Iron time yields (FTY) were expressed as moles of CO_2 converted per gram of iron (determined from XRF analysis) per second.

3. Results and Discussion

3.1. CO_2 hydrogenation over iron-molybdenum catalysts

Before the catalytic performance tests, the catalysts were firstly activated with CO. Then, they were exposed to the flow of CO_2 and hydrogen. The catalytic data of different iron molybdates are shown in **Figures 1, S1-2** and **Table 1**. The CO_2 conversion over all the catalysts displays an induction period, which presents a rapid increase in the CO_2 conversion. The CO_2 conversion then reaches a relative steady value. The non-promoted FeMo catalyst shows a CO_2 conversion of 16.8 % and thus corresponding to a FTY of 5.8×10^{-5} $mol_{CO2}/g_{Fe}s$. The main product was CH_4 (88.5 %) along with a very small amounts of light olefins ($C_{2\text{-}4}^{=}$, selectivity of 2.6 %). The reaction rate expressed as FTY of FeMoX (X = Li, Na, K, Rb and Cs) was a function of alkaline metal. The Li- and Na-modified catalysts showed higher catalytic activity than the unpromoted FeMo. In contrast, under the same space velocity, iron catalysts doped with other alkaline metals show similar CO_2 conversions of ~10 %, which are lower than FeMo catalyst. Higher reaction rate was observed over the catalysts promoted with high electronegative alkaline metals (Li and Na), while the reaction rate drops as the electronegativity of the promoting metal decreases. The CO_2 hydrogenation rate over iron catalysts promoted with alkaline metals is similar to the

promoted CoCu/TiO_2 catalyst, where the activity of Li-CoCu/TiO_2 outperformed other CoCu catalysts. The effect was attributed to the geometric effect of Li with a smaller ion radius on the active sites and its strong polarization ability[15], compared to other alkaline metals.

Figure S1b-d shows hydrocarbon selectivity over iron molybdates as a function of CO_2 conversion. The C_{2+} product selectivity (light olefins and $C5^+$ products) at similar CO_2 conversion of about 15 %, increases in the order of Li < Na < K < Rb < Cs (**Figure 1d** and **Figure S2**). The increase in light olefin and C_{5+} hydrocarbon selectivity occurs at the expense of methane. Interestingly, compared to unpromoted FeMo, promotion with alkaline metals (K, Rb and Cs) increases the selectivity to light olefins by a factor of ~ 5.5. In particular, FeMoCs exhibits the lowest selectivity to CH_4 (45.3%) among the catalysts and remarkably higher selectivity to light olefins (29.7 %) (**Table 1**). Since FeMoCs produces more light olefins than other catalysts, it has been tested for a longer time on stream (TOS) of 50 h (**Figure 1e**). After the stabilization for ~15 h, the CO_2 conversion was constant at steady state with an average value of ~13 %. The selectivity to light olefins over FeMoCs was constant after stabilization and reaches ~29.8%. Based on the above catalytic results, we could conclude that the alkaline metals exert significant promoting effects on both CO_2 conversion and product selectivity of iron molybdate catalysts.

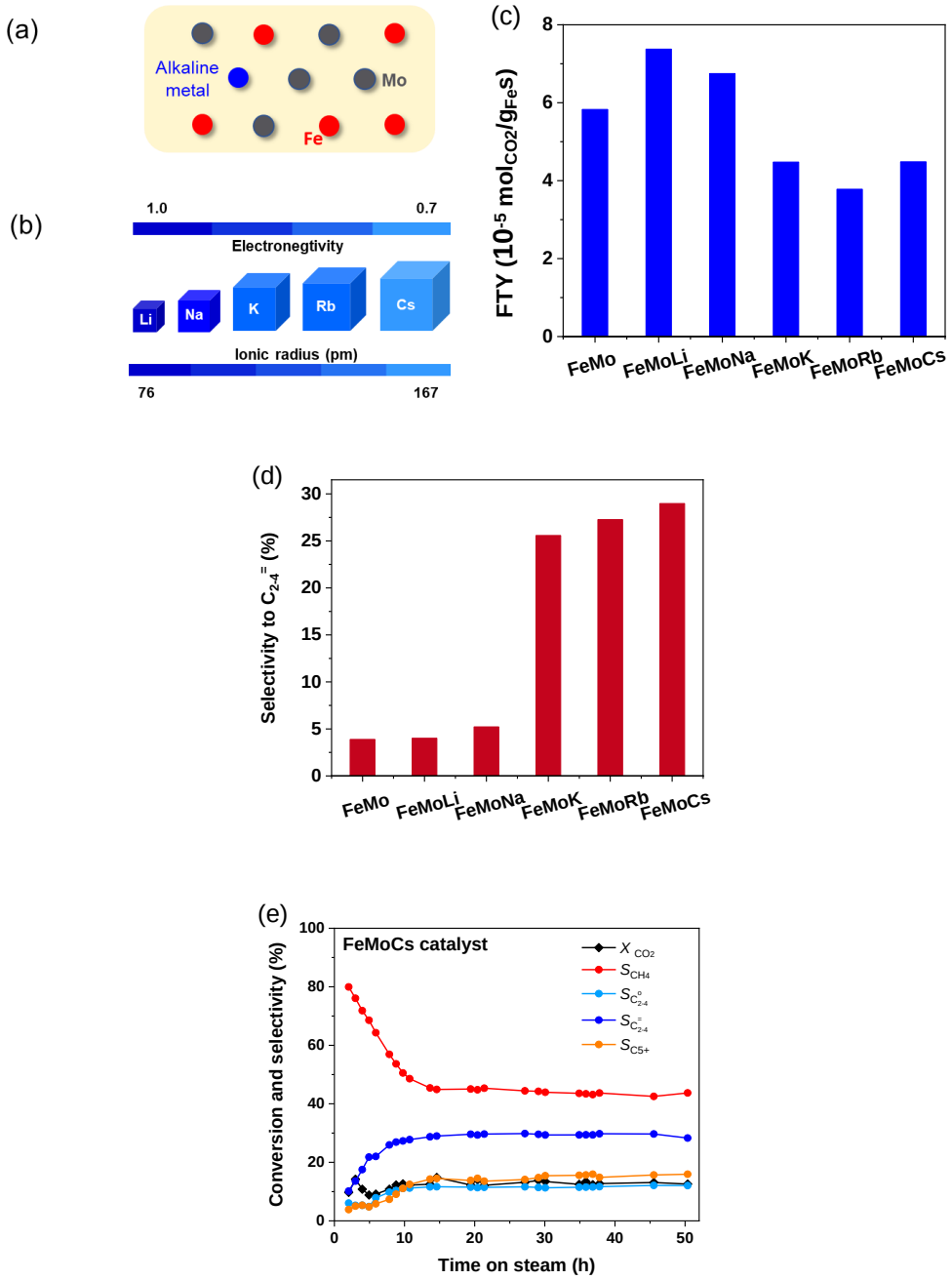

Figure 1. CO_2 hydrogenation performances of iron molybdate catalysts ($H_2/CO_2/N_2$ at 12/4/1, 9300 ml $g_{catalyst}^{-1}$ $hour^{-1}$, 10 bar, 350 °C). (a) scheme of catalysts composition. (b) Pauling electronegativity and ironic radius of alkaline metals. (c) iron time yield (FTY, TOS = 22h). (d) light olefin selectivity ($S_{C2-4}^{=}$) at similar CO_2 conversion of ~15%. (e) CO_2 conversion (X_{CO2}) and hydrocarbons selectivity as a function of TOS over FeMoCs.

Table 1. CO_2 hydrogenation over iron molybdate catalysts (110 mg catalyst, $H_2/CO_2/N_2$ at 12/4/1, 9300 ml $g_{catalyst}^{-1}$ $hour^{-1}$, 10 bar, 350 °C, TOS = 22 h).

Catalyst	X_{CO2} (%)	S_{CO} (%)	CO-free product selectivity (%)			
			S_{CH4}	S_{C2-4}^{o}	$S_{C2-4}^{=}$	S_{C5+}
FeMo	16.8	52.9	88.5	8.5	2.6	0.3
FeMoLi	22.9	38.4	86.6	6.2	5.7	1.4
FeMoNa	22.2	47.8	79.7	6.4	11.9	2.0
FeMoK	13.9	53.8	58.1	4.5	31.1	6.3
FeMoRb	10.2	36.7	56.8	3.2	28.2	11.9
FeMoCs	12.1	41.0	45.3	11.5	29.7	13.6

3.2. Catalyst characterization

A wide range of characterization techniques were used to investigate the physicochemical properties of iron catalysts. All the samples contain (**Table S1**) similar amounts of iron (7.3-8.9 %) and molybdenum (13.3-15.5 %). The XRD patterns of calcined, activated and spent iron molybdate catalysts are shown in **Figure 2**. The XRD patterns of calcined FeMo non-promoted and alkaline metal promoted FeMoX catalysts (X = Li, Na, K, Rb and Cs) display diffraction peaks at 2θ 13.8°, 15.3°, 19.4°, 20.4°, 22.9°, 25.1°, 25.7°, 27.5°, 30.1°, 31.4° and 34°, which correspond to the $Fe_2(MoO_4)_3$ phase (JCPDS 04-007-2787), while the peaks at 12.9° and 23.3° are attributed to orthorhombic α-MoO_3 (JCPDS 01-080-3491). No peaks attributed to iron oxides were detected in the calcined iron molybdates, probably because of their high dispersion. In addition, no diffraction peaks associated with the alkali metals are observed for all FeMoX samples, which may be due to their low concentrations.

The catalyst activation under carbon monoxide results in the modification of XRD patterns. In addition to the $Fe_2(MoO_3)_4$ and MoO_3 peaks, new diffraction peaks are observed at 13.1°, 26.3°, and 33.7°, which correspond $FeMoO_4$ (JCPDS 00-022-0628). This new phase could be formed by reduction of Fe^{3+} to Fe^{2+} species during the CO activation. The XRD patterns for catalysts after the CO_2 hydrogenation were also recorded. Most of the diffraction peaks related to $Fe_2(MoO_3)_4$ and $FeMoO_4$ weaken or disappear after the reaction, while the spent catalysts exhibit diffraction peaks at 2θ angles around 42.9° that could be attributed[16] to iron carbides formed during the reaction.

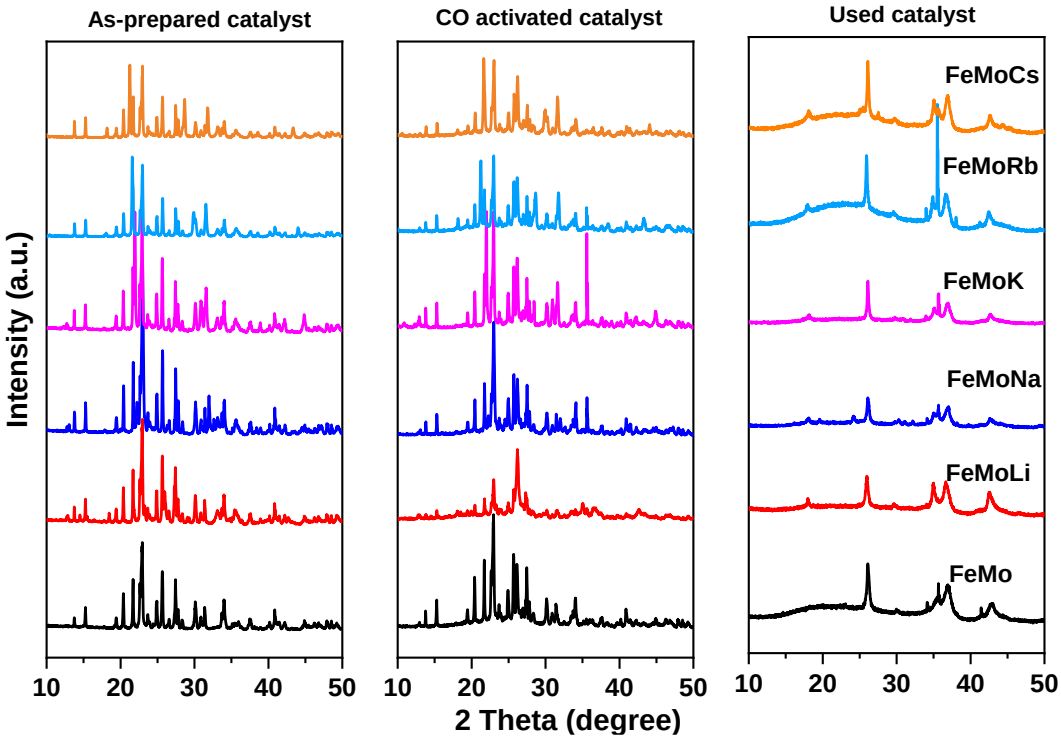

Figure 2. XRD of as-prepared, CO activated, and used iron molybdate catalysts.

High-resolution STEM and EDX elemental mapping were used to characterize FeMo and FeMoCs catalysts at different stages of preparation, activation and reaction. The

calcined FeMo are composed of oxide particles of around 15 nm **(Figures 3a** and **Figure S3).** Interestingly, after the CO activation, the iron and molybdenum species became spatially separated. The segregation was caused by CO reduction and carbidisation. However, these two components merge again during the CO_2 hydrogenation. In addition, carbon deposition was observed over the spent FeMo sample (**Figure S4**). Remarkably, calcined FeMoCs showed domains with different composition (**Figure 4** and **Figure S5**), which are iron molybdates (marked as yellow circle), iron oxides (green square) and molybdenum oxides (blue square). This suggests that the alkaline metal promotes the phase separation during the calcination. The followed CO activation and reaction condition did not significant change the morphology and phase composition of FeMoCs catalyst.

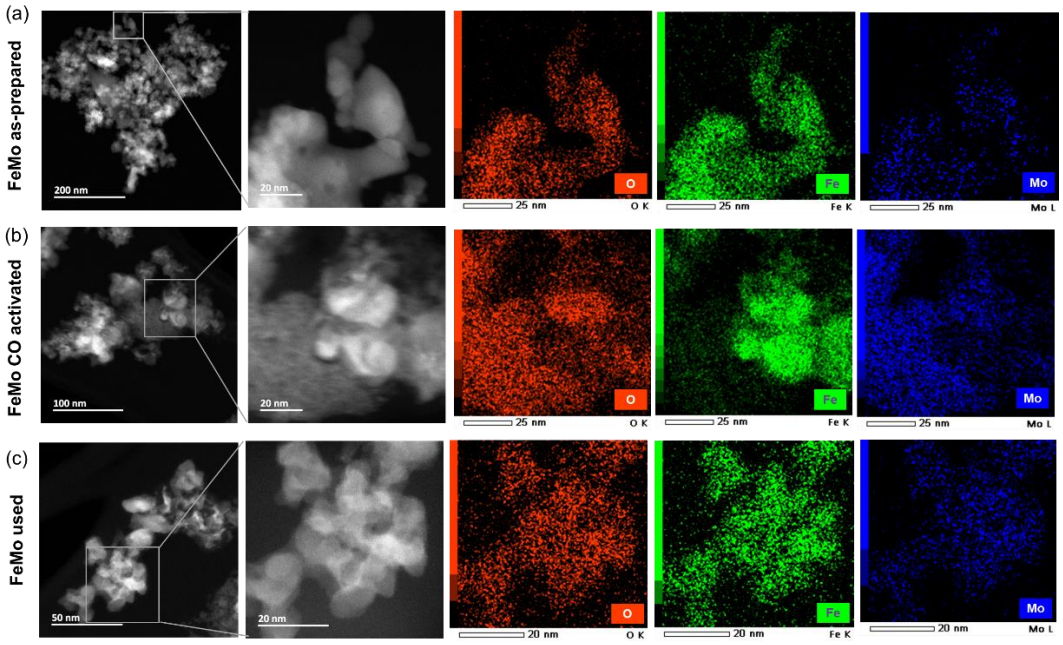

Figure 3. STEM-ADF (Annular Dark Field) and elemental mapping images of the calcined, activated and spent FeMo (a, b and c).

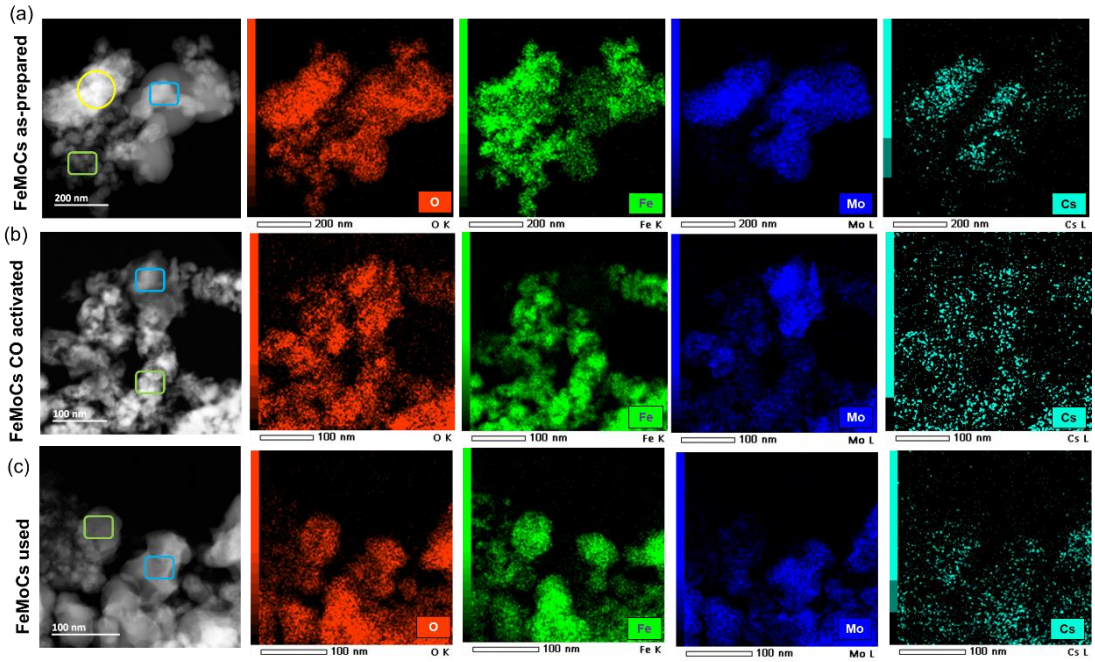

Figure 4. STEM-ADF and elemental mapping images of the calcined, activated and spent FeMoCs (a, b and c)

Previous reports suggest[16, 32] that the surface basicity of catalysts may play an important role in the CO_2 hydrogenation process. CO_2-TPD was used to investigate the surface basic properties of iron molybdate catalysts. **Figure 5** and **Table S1** show very low amount of adsorbed CO_2 (2.8 µmol/g) over unpromoted FeMo. The CO_2-TPD profile of FeMo displays only a broad peak located at 550-700 °C, which corresponds to the CO_2 desorption from the strong basic sites. Promotion with alkali metals leads to the appearance of weaker basic sites with TPD peaks at 300-500 °C, along with high temperature peaks. The catalysts promoted with alkaline metals exhibit a higher quantity of desorbed CO_2 (3.4-6.1 vs. 2.8 µmol/g for the unpromoted counterpart). The total amount of basic sites increases in the following order of FeMoLi < FeMo < FeMoNa < FeMoK ≈ FeMoCs < FeMoRb. Interestingly, a fraction of weak acid sites (**Table S1, SI**) was higher in the catalysts promoted with Li^+ and Na^+.

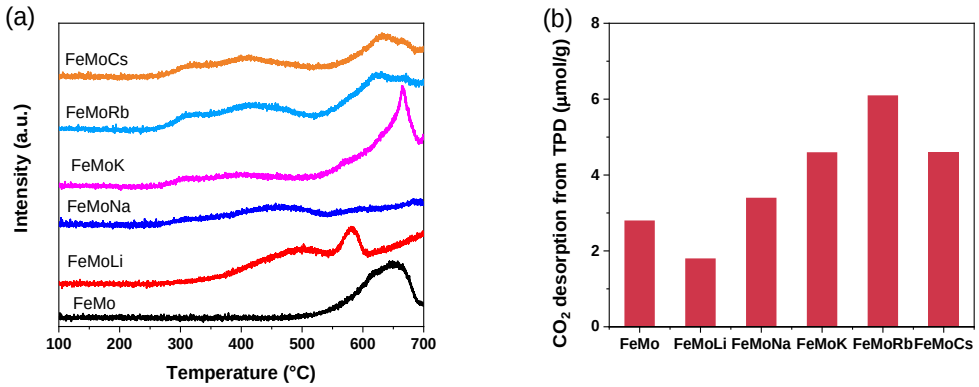

Figure 5. CO_2-TPD profiles (a) and CO_2 desorption amount (b) measured over iorn catalysts.

The catalyst reducibility was evaluated by H_2-TPR (**Figure 6** and **Table S1**). No hydrogen consumption below 400 °C was observed for all the catalysts. Non-promoted FeMo showed three broad TPR peaks at 657, 800 and 962 °C. These peaks are associated with reduction of iron (III) molybdate: $Fe_2(MoO_4)_3 \rightarrow FeMoO_4 + Mo_4O_{11} \rightarrow Fe_2Mo_3O_8 + Fe_3O_4 \rightarrow$ Fe-Mo alloy[17, 33]. This interpretation of H_2-TPR profiles is consistent with previous report[17] for bimetallic Fe-Mo/Al_2O_3 catalyst. The H_2-TPD profile of FeMoLi only slightly changes compared with that of FeMo. This suggests that Li has a weak effect on the reducibility of iron molybdate. In contrast, the promotion of iron molybdates with K, Rb and Cs shifts the dominant reduction peak to lower temperature compared to FeMo (739 ~ 766 °C vs. 800 °C). This suggests that K, Rb and Cs enhance the catalyst reducibility. Interestingly, in the CO_2 hydrogenation, higher C_{2+} hydrocarbon selectivity was reached over the catalysts with better reducibility. Iron carbides are usually considered active species for CO hydrogenation over iron-based catalysts[34, 35]. The increased reducibility of iron molybdates would allow more iron carbides to be produced during the catalyst activation and reaction.

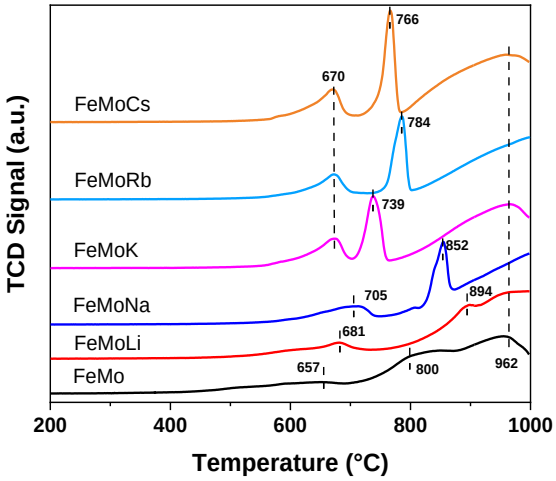

Figure 6. H_2-TPR profiles of iron molybdate catalysts.

3.3. Evolution of the catalyst structure during activation and reaction

The evolution of catalyst structure of iron catalysts was investigated using *in-situ* Mössbauer spectrometry and *operando* XAS. The Mössbauer spectra were measured after the catalyst exposure to reacting gas (CO during activation or H_2/CO_2 during the reaction) and then after rapid cooling to -153 °C (**Figure 7**). The conditions used in the treatment of catalyst with gas during the *in-situ* Mössbauer spectrometric measurements were similar to those in the catalytic tests. The Mössbauer spectra are displayed in **Figure 7**. The Mössbauer fit parameters of calcined catalysts and catalyst exposed to CO and $CO_2 + H_2$ are given in **Table 2**.

The spectra of calcined samples reveal the presence of both hematite and $Fe_2(MoO_4)_3$ iron (III) molybdate phases (**Table 2**). The Mossbauer results are consistent with the XRD data that also showed $Fe_2(MoO_4)_3$ as the main phase in the calcined catalysts. The weight ratio between hematite and ferric molybdate is different in FeMo and FeMoCs.

Introduction of alkaline metals increases the fraction of $Fe_2(Mo_3O)_4$ phase. In addition, the hematite hyperfine field is slightly smaller in FeMoCs compared to the FeMo sample, indicating Cs incorporation in the crystalline structure or better dispersion of the Fe species in FeMoCs.

Then, both FeMo and FeMoCs catalysts were *in-situ* activated in the CO flow (350 °C, 1 bar) and exposed to the reaction gas mixture (H_2/CO_2 = 3) at 350 °C and 10 bar. Note that the Mössbauer spectra of the catalysts during the activation and reaction are rather different from the calcined catalysts. After the CO activation, iron carbides and $FeMoO_4$ species were observed in both samples. These results indicate partial reduction of $Fe_2(MoO_4)_3$ and carbidisation of iron oxide. Note that the total amount of iron carbides is comparable in FeMo and FeMoCs (23% vs. 19%).

After the activation in CO, the catalysts were exposed to H_2/CO_2 reacting mixture. **Figure 7** also shows the *in-situ* Mössbauer spectra of catalysts measured during the reaction. In both catalysts, all the remaining $Fe_2(MoO_4)_3$ species were fully reduced to $FeMoO_4$ under the reaction gas atmosphere. In addition, Fe-Mo alloy-like phase was formed. Remarkably, FeMoCs contains a larger amount of Fe-Mo alloy than FeMo after the CO_2 hydrogenation (32% vs. 24%) (**Table 2**). Besides, the fraction of iron carbide slightly increases during the reaction. The Mössbauer results are therefore indicative of reduction of both molybdenum and iron during the catalyst activation and partial carbidisation of iron. The reduction processes seem to be enhanced in the presence of Cs and produces a higher fraction of Fe-Mo alloy. The in-situ Mössbauer results are consistent with the TPR profiles of FeMo and FeMoCs catalysts.

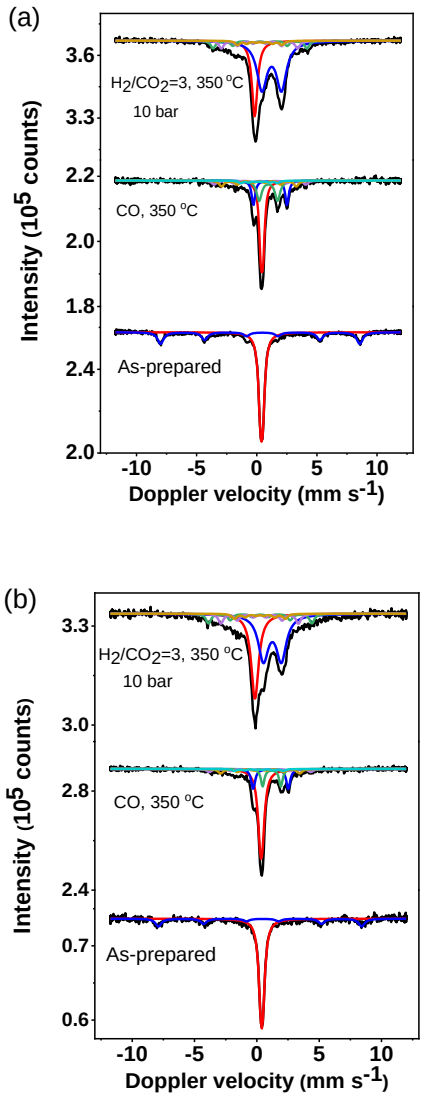

Figure 7. *In-situ* Mössbauer spectra of FeMo (a) and FeMoCs (b) samples. The measurements were performed after rapid cooling to -153 °C.

Table 2. The Mössbauer fitted parameters of the iron catalysts, obtained at -153 °C*.

Sample/ Treatment	IS ($mm \cdot s^{-1}$)	QS ($mm \cdot s^{-1}$)	Hyperfine field (T)	Γ ($mm \cdot s^{-1}$)	Phase	Spectral contribution (%)
FeMo As-prepared	0.37	-0.17	51.5	0.59	α-Fe_2O_3	34
	0.40	0.19	-	0.41	$Fe_2(MoO_4)_3$	66
FeMo CO, 350 ℃	0.26	-	23.7	0.46	χ-Fe_5C_2 (I)	8
	0.18	-	19.3	0.46	χ-Fe_5C_2 (II)	11
	0.19	-	11.0	0.46	χ-Fe_5C_2 (III)	4
	0.43	0.19	-	0.35	$Fe_2(MoO_4)_3$	40
	1.12	2.79	-	0.34	β-$FeMoO_4$	17
	0.96	1.53	-	0.50	α-$FeMoO_4$	20
FeMo H_2/CO_2=3 350 ℃, 10 bar	0.27	-	24.2	0.46	χ-Fe_5C_2 (I)	9
	0.22	-	19.7	0.46	χ-Fe_5C_2 (II)	9
	0.24	-	11.5	0.46	χ-Fe_5C_2 (III)	4
	-0.17	-	-	0.56	Fe-Mo	24
	1.24	1.62	-	1.00	α-$FeMoO_4$	54
FeMoCs As-prepared	0.36	-0.20	50.7	0.59	α-Fe_2O_3	25
	0.40	0.15	-	0.45	$Fe_2(MoO_4)_3$	75
FeMoCs CO, 350 ℃	0.25	-	25.3	0.47	χ-Fe_5C_2 (I)	6
	0.20	-	19.7	0.47	χ-Fe_5C_2 (II)	9
	0.16	-	12.2	0.47	χ-Fe_5C_2 (III)	4
	0.40	0.15	-	0.50	$Fe_2(MoO_4)_3$	53
	1.11	2.81	-	0.37	β-$FeMoO_4$	16
	1.20	1.46	-	0.34	α-$FeMoO_4$	12
FeMoCs H_2/CO_2=3 350 ℃, 10 bar	0.26	-	25.6	0.47	χ-Fe_5C_2 (I)	9
	0.21	-	19.3	0.47	χ-Fe_5C_2 (II)	9
	0.20	-	12.7	0.47	χ-Fe_5C_2 (III)	5
	-0.15	-	-	0.72	Fe-Mo	32
	1.24	1.44	-	0.98	α-$FeMoO_4$	45

*Experimental uncertainties: Isomer shift: I.S. ± 0.02 mm s^{-1}; Quadrupole splitting: Q.S. ± 0.02 mm s^{-1}; Line width: Γ ± 0.03 mm s^{-1}; Hyperfine field: ± 0.1 T; Spectral contribution: ± 3%.

The evolution of the structure of FeMo and FeMoRb catalysts under the reaction conditions was further characterized by *operando* XAS. FeMoRb was chosen because of the possibility to measure in the same experiments the absorption edges of Fe, Mo, and Rb.[36]

First, we measured the Mo, Fe and Rb K absorption edges of FeMo, FeMoRb and FeMoCs catalysts after calcination along with the spectra of several reference compounds (**Figure S6 a, c, Figure S7**). The XANES spectra (**Figure S6a**) of calcined catalysts at the Mo K-edge exhibit a pre-edge peak at around 19 995 eV, which is attributed to the dipole-forbidden/quadrupole-allowed 1s–4d transition and is primarily associated to tetrahedral geometry of Mo. Another peak at 20 015 eV is assigned to the dipole-allowed 1s–5p transition, which is considered as characteristic feature of Mo species with a octahedral/distorted octahedral geometry [37]. Three iron samples show spectra similar to those of reference MoO_3 and $Fe_2(MoO_4)_3$, indicating that Mo in the catalysts possesses both tetrahedral and octahedral geometry. Their corresponding Fourier transform (FT) EXAFS moduli are shown in **Figure S6b**. In agreement with the literature, an intensive peak at 1.35 Å is assigned to the first shell Mo-O1 coordination[37], which suggests the presence of tetrahedral Mo-O species in $Fe_2(MoO_4)_3$. In addition, the Fe K-edge XANES and FT EXAFS moduli of the calcined FeMo, FeMoRb and FeMoCs catalysts show similarity with reference $Fe_2(MoO_4)_3$ and Fe_2O_3. This suggests that the Fe in the calcined catalysts mainly presents as $Fe_2(MoO_4)_3$ and Fe_2O_3 phases. This observation agrees with the Mössbauer results. The XANES spectra of FeMoRb catalyst at the Rb K-absorption edge are displayed in **Figure S7**. In the fresh calcined catalyst, rubidium is present as a mixture of rubidium hydroxide and carbonate. After conducting the CO_2 hydrogenation, Ru tends to agglomerate in rubidium oxide.

Figure 8a shows that *operando* Mo K-edge XANES spectra of FeMoCs during CO activation and CO_2 hydrogenation show a gradual shift of the edge position to lower energies, from around 20 008 to 20 002 eV. This shift indicates continuous reduction of Mo in the presence of CO. Besides, the intensity of pre-edge peaks decreased and a peak around 20 015 eV increases simultaneously with the time. The spectrum evolution suggests reduction of $Fe_2(MoO_4)_3$ and MoO_3 to $FeMoO_4$ and MoO_2. After the CO_2 hydrogenation, the pre-edge peak completely disappears and the XANES spectra get very similar to that of reference MoO_2. The Mo (VI) species seem to be completely reduced to Mo(IV) during the reaction. The corresponding Fourier transform Mo K-EXAFS moduli during the CO activation and CO_2 hydrogenation are shown in **Figure 8b**. During the CO activation and CO_2 hydrogenation, the intensity of the peak at 1.6 Å attributed to Mo-O1 tetrahedral coordination gradually decreases and completely disappears after the CO_2 hydrogenation.

Figure 8 c and **d** shows the *operando* Fe K-edge XANES and EXAFS spectra measured during CO activation and CO_2 hydrogenation. Initially, the Fe K-edge absorption edge was observed at 7132 eV. After the CO activation and CO_2 hydrogenation, the spectra exhibit a gradual shift towards lower energy indicating a change in the average oxidation state of Fe to lower oxidation state, mainly corresponding to the formation of $FeMoO_4$[37] and iron carbides.

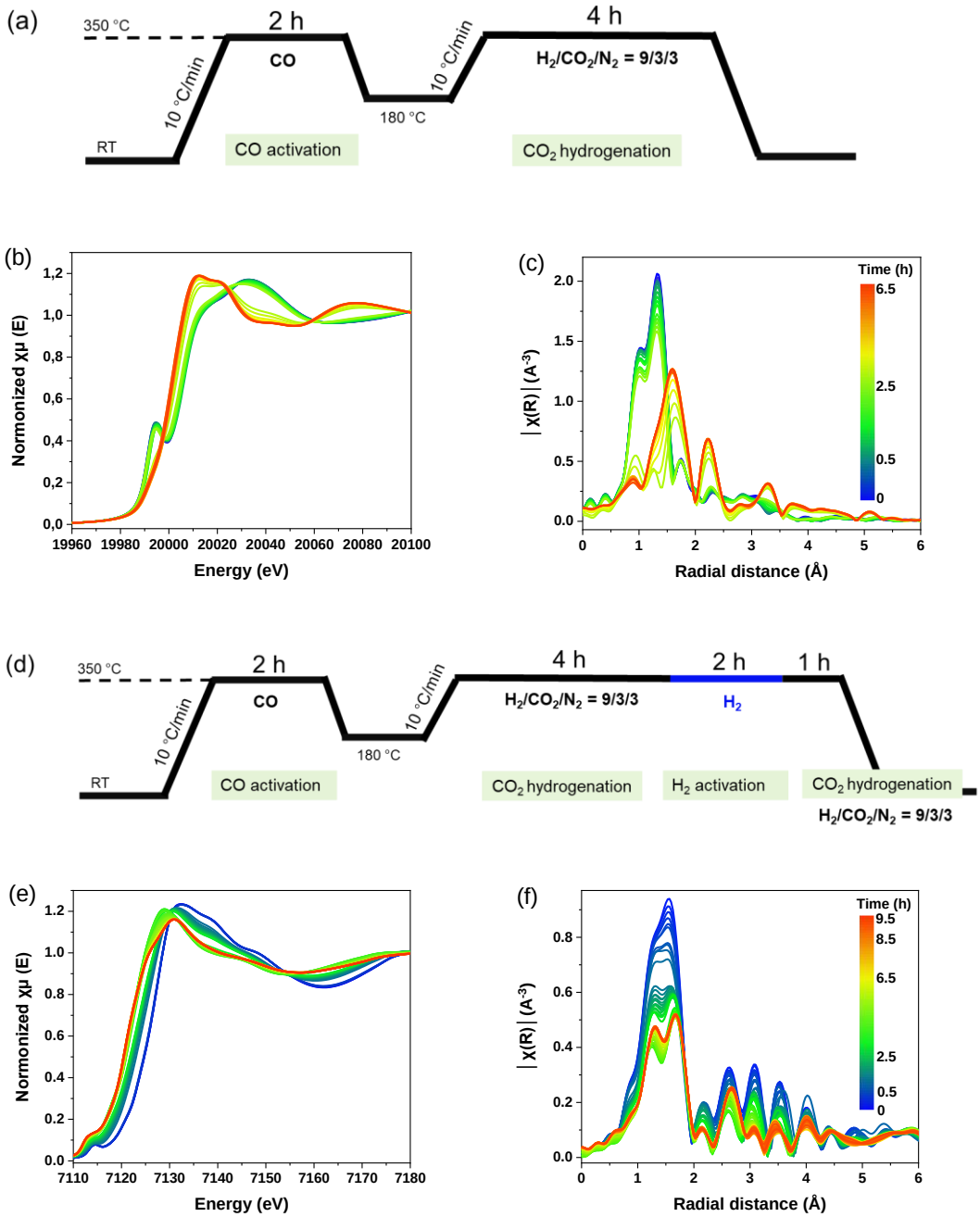

Figure 8. (a, d) procedures for in-situ XAS experiments. (b, e) *In-situ* Mo and Fe K-edge XANES spectra and (c, f) k^2-weighted Fourier transformed EXAFS spectra of FeMoRb catalyst during CO activation and CO_2 hydrogenation reaction.

The contributions of the different phases obtained from liner combination fitting (LCF) analysis of the XANES spectra at the Mo and Fe K-edge during CO activation and CO_2 hydrogenation reaction are shown in **Figure 9** and **Figure S8**. LCF was performed using standard spectra of $Fe_2(MoO_4)_3$, MoO_3, MoO_2, Fe_2O_3, Fe_3O_4, FeO, Fe_3C and FeC.

Figure 9a shows that the Mo species started to reduce when the temperature increased to 350 °C under CO, the fractions of MoO_3 and MoO_2 increase at the expense of $Fe_2(MoO_4)_3$. During the CO activation, the fraction of MoO_3 reaches a maximum and then decreases while the quantifiMoO_2 kept increasing. The amount of these three Mo phases did not have significant variation during the CO_2 hydrogenation stage. Finally, after reaction, contributions from MoO_3 and MoO_2 were observed to be 23% and 77% respectively. LCF analysis (**Figure 9b**) showed that the initial composition of the calcined FeMoRb was 68.8% $Fe_2(MoO_4)_3$ and 31.2% Fe_2O_3 which is similar to the Fe phases composition of the Mössbauer results obtained from FeMoCs (75% $Fe_2(MoO_4)_3$, 25% Fe_2O_3). During the CO activation, both $Fe_2(MoO_4)_3$ and Fe_2O_3 contents decreased. Fe_3O_4 and Fe_3C phases were intermediates and their contributions were found to decrease, while the fractions of FeO and FeC increase.

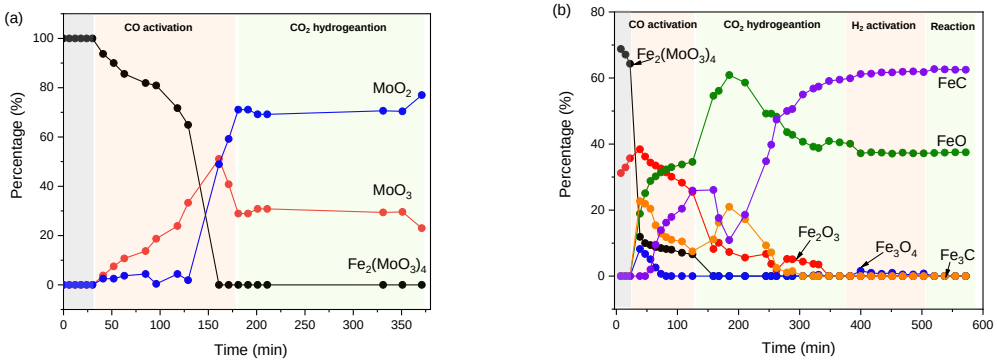

Figure 9. Evolution of Mo (a) and Fe (b) phase compositions during the CO activation and CO_2 hydrogenation reaction.

Table 3. Catalytic data of FeMoRb catalysts in *in-situ* XAS experiment (10 mg catalyst, $H_2/CO_2/N_2$ at 9/3/3, 6 bar, 350°C).

	TOS	X_{CO2}	S_{CO}	CO-free product selectivity (%)			
	(min)	(%)	(%)	S_{CH4}	$S_{C2\text{-}4}{}^{o}$	$S_{C2\text{-}4}{}^{=}$	$S_{C5}{}^{+}$
Mo K-edge	46	8.0	97.6	78.7	8.2	7.4	5.8
	230	8.5	98.3	76.5	7.2	10.3	6.0
Fe K-edge	47	6.4	97.0	83.1	5.1	7.0	4.7
	235	7.1	97.9	78.2	5.9	8.4	7.5

The *operando* XAS were measured simultaneously with chemical analysis of the reaction products (**Table S3**). The CO_2 conversion in the *in-situ* XAS cell leads to the production of CO and hydrocarbons. Different from the catalytic results obtained from the conventional fixed-bed set up, lower CO_2 conversion was observed in the *in-situ* XAS experiments with a much higher selectivity to CO. This discrepancy may be due to the lower reaction pressure and shorter activation time of the catalyst in CO due to technical limitations in *in-situ* synchrotron experiments compared to traditional catalysis tests.

Kondratenko[32] et.al proposed that in the CO_2 hydrogenation over iron catalysts, the CO_2 activation ability expressed by effective CO_2 adsorption and dissociation rate constants directly influences the CO_2 conversion activity and product selectivity. They also pointed out that too strong CO_2 adsorption is unfavourable for the catalyst activity. Following the trends between CO_2 transformation activity and surface basic properties of iron molybdate catalysts, we may conclude that the alkali metals resulted in lower surface basicity of iron molybdate catalysts would more facilize the CO_2 activation and further the CO_2 hydrogenation activity.

4. Conclusion

A series of iron-molybdenum catalysts promoted with alkaline metals was prepared for CO_2 hydrogenation. The calcined catalysts contain iron (III) molybdate, MoO_3 and iron oxide species. Introduction of alkaline metals results in a greater amount of basic sites. Higher fraction of weak basic sites was observed with Li and Na promoters. The presence of Cs and Rb increases the catalyst reducibility. Electronegativity of alkaline metals seems to be a principal descriptor of the catalytic properties. The presence of high electronegative alkaline promoters favours CO_2 conversion rate, while the low electronegative alkaline metals such as Cs and Rb exhibit low reaction rate but show higher light olefin selectivity. The *in-situ* techniques employed in this work showed gradual reduction of molybdenum and iron to $FeMoO_4$ and MoO_2 and respectively FeO. The presence of Fe-Mo ally was also detected. A part of iron is carbidised to a mixture of iron carbides under catalyst activation and during catalytic reaction.

Acknowledgments

We thank Olivier Gardoll and Dr. Joelle Thuriot-Roukos for help in TPR-TPD and XRF characterization. The authors acknowledge financial support from the French National Research Agency (Multiprobe project, ANR-20-CE42-0007). We thank the Swiss Light Source and Super XAS beamline for the synchrotron measurements.

References

1. Canadell, J. G.; Le Quéré, C.; Raupach, M. R.; Field, C. B.; Buitenhuis, E. T.; Ciais, P.; Conway, T. J.; Gillett, N. P.; Houghton, R.; Marland, G., Contributions to accelerating atmospheric CO_2 growth from economic activity, carbon intensity, and efficiency of natural sinks. *Proceedings of the National Academy of Sciences* **2007,** *104* (47), 18866-18870.

2. Hoegh-Guldberg, O.; Mumby, P. J.; Hooten, A. J.; Steneck, R. S.; Greenfield, P.; Gomez, E.; Harvell, C. D.; Sale, P. F.; Edwards, A. J.; Caldeira, K., Coral reefs under rapid climate change and ocean acidification. *Science* **2007,** *318* (5857), 1737-1742.

3. Hopkins, F. E.; Suntharalingam, P.; Gehlen, M.; Andrews, O.; Archer, S. D.; Bopp, L.; Buitenhuis, E.; Dadou, I.; Duce, R.; Goris, N., The impacts of ocean acidification on marine trace gases and the implications for atmospheric chemistry and climate. *Proceedings of the Royal Society A* **2020,** *476* (2237), 20190769.

4. Gao, W.; Liang, S.; Wang, R.; Jiang, Q.; Zhang, Y.; Zheng, Q.; Xie, B.; Toe, C. Y.; Zhu, X.; Wang, J., Industrial carbon dioxide capture and utilization: state of the art and future challenges. *Chemical Society Reviews* **2020,** *49* (23), 8584-8686.

5. Zhang, Z.; Pan, S.-Y.; Li, H.; Cai, J.; Olabi, A. G.; Anthony, E. J.; Manovic, V., Recent advances in carbon dioxide utilization. *Renewable and Sustainable Energy Reviews* **2020,** *125*, 109799.

6. Wang, F.; Harindintwali, J. D.; Yuan, Z.; Wang, M.; Wang, F.; Li, S.; Yin, Z.; Huang, L.; Fu, Y.; Li, L., Technologies and perspectives for achieving carbon neutrality. *The Innovation* **2021,** *2* (4), 100180.

7. Mandal, S. C.; Das, A.; Roy, D.; Das, S.; Nair, A. S.; Pathak, B., Developments of the heterogeneous and homogeneous CO_2 hydrogenation to value-added C_{2+}-based hydrocarbons and oxygenated products. *Coordination Chemistry Reviews* **2022,** *471*, 214737.

8. Zhang, W.; Jin, Z.; Chen, Z., Rational-Designed Principles for Electrochemical and Photoelectrochemical Upgrading of CO_2 to Value-Added Chemicals. *Advanced Science* **2022,** *9* (9), 2105204.

9. Chernyak, S. A.; Corda, M.; Dath, J. P.; Ordomsky, V. V.; Khodakov, A. Y., Light olefin synthesis from a diversity of renewable and fossil feedstocks: state-of the-art and outlook. *Chemical Society Reviews* **2022,** *51* (18), 7994-8044.

10. Todić, B.; Ordomsky, V. V.; Nikačević, N. M.; Khodakov, A. Y.; Bukur, D. B., Opportunities for intensification of Fischer–Tropsch synthesis through reduced formation of methane over cobalt catalysts in microreactors. *Catalysis Science & Technology* **2015,** *5* (3), 1400-1411.

11. Gholami, Z.; Tišler, Z.; Rubáš, V., Recent advances in Fischer-Tropsch synthesis using cobalt-based catalysts: A review on supports, promoters, and reactors. *Catalysis Reviews* **2021,** *63* (3), 512-595.

12. Chen, Y.; Wei, J.; Duyar, M. S.; Ordomsky, V. V.; Khodakov, A. Y.; Liu, J., Carbon-based catalysts for Fischer–Tropsch synthesis. *Chemical Society Reviews* **2021,** *50* (4), 2337-2366.

13. Barrios, A. J.; Gu, B.; Luo, Y.; Peron, D. V.; Chernavskii, P. A.; Virginie, M.; Wojcieszak, R.; Thybaut, J. W.; Ordomsky, V. V.; Khodakov, A. Y., Identification of efficient promoters and selectivity trends in high temperature Fischer-Tropsch synthesis over supported iron catalysts. *Applied Catalysis B: Environmental* **2020,** *273*, 119028.

14. Shi, Z.; Yang, H.; Gao, P.; Li, X.; Zhong, L.; Wang, H.; Liu, H.; Wei, W.; Sun, Y., Direct conversion of CO_2 to long-chain hydrocarbon fuels over K-promoted $CoCu/TiO_2$ catalysts. *Catalysis Today* **2018,** *311*, 65-73.

15. Shi, Z.; Yang, H.; Gao, P.; Chen, X.; Liu, H.; Zhong, L.; Wang, H.; Wei, W.; Sun, Y., Effect of alkali metals on the performance of $CoCu/TiO_2$ catalysts for CO_2 hydrogenation to long-chain hydrocarbons. *Chinese Journal of Catalysis* **2018,** *39* (8), 1294-1302.

16. Barrios, A. J.; Peron, D. V.; Chakkingal, A.; Dugulan, A. I.; Moldovan, S.; Nakouri, K.; Thuriot-Roukos, J.; Wojcieszak, R.; Thybaut, J. W.; Virginie, M.; Khodakov, A. Y., Efficient Promoters and Reaction Paths in the CO_2 Hydrogenation to Light Olefins over Zirconia-Supported Iron Catalysts. *ACS Catalysis* **2022,** *12* (5), 3211-3225.

17. Kharaji, A. G.; Shariati, A.; Takassi, M. A., A novel γ-alumina supported Fe-Mo bimetallic catalyst for reverse water gas shift reaction. *Chinese Journal of Chemical Engineering* **2013,** *21* (9), 1007-1014.

18. Routray, K.; Zhou, W.; Kiely, C. J.; Grünert, W.; Wachs, I. E., Origin of the synergistic interaction between MoO_3 and iron molybdate for the selective oxidation of methanol to formaldehyde. *Journal of Catalysis* **2010,** *275* (1), 84-98.

19. House, M. P.; Carley, A. F.; Echeverria-Valda, R.; Bowker, M., Effect of varying the cation ratio within iron molybdate catalysts for the selective oxidation of methanol. *The Journal of Physical Chemistry C* **2008,** *112* (11), 4333-4341.

20. Peron, D. V.; Barrios, A. J.; Taschin, A.; Dugulan, I.; Marini, C.; Gorni, G.; Moldovan, S.; Koneti, S.; Wojcieszak, R.; Thybaut, J. W., Active phases for high temperature Fischer-Tropsch

synthesis in the silica supported iron catalysts promoted with antimony and tin. *Applied Catalysis B: Environmental* **2021,** *292*, 120141.

21. Gu, B.; Peron, D. V.; Barrios, A. J.; Bahri, M.; Ersen, O.; Vorokhta, M.; Šmíd, B.; Banerjee, D.; Virginie, M.; Marceau, E.; Wojcieszak, R.; Ordomsky, V. V.; Khodakov, A. Y., Mobility and versatility of the liquid bismuth promoter in the working iron catalysts for light olefin synthesis from syngas. *Chemical Science* **2020,** *11* (24), 6167-6182.

22. Kalz, K. F.; Kraehnert, R.; Dvoyashkin, M.; Dittmeyer, R.; Gläser, R.; Krewer, U.; Reuter, K.; Grunwaldt, J. D., Future challenges in heterogeneous catalysis: understanding catalysts under dynamic reaction conditions. *ChemCatChem* **2017,** *9* (1), 17-29.

23. Zhang, X.; Han, S.; Zhu, B.; Zhang, G.; Li, X.; Gao, Y.; Wu, Z.; Yang, B.; Liu, Y.; Baaziz, W., Reversible loss of core–shell structure for Ni–Au bimetallic nanoparticles during CO_2 hydrogenation. *Nature Catalysis* **2020,** *3* (4), 411-417.

24. Foster, A. J.; Lobo, R. F., Identifying reaction intermediates and catalytic active sites through in situ characterization techniques. *Chemical Society Reviews* **2010,** *39* (12), 4783-4793.

25. Li, X.; Yang, X.; Zhang, J.; Huang, Y.; Liu, B., In situ/operando techniques for characterization of single-atom catalysts. *ACS Catalysis* **2019,** *9* (3), 2521-2531.

26. Timoshenko, J.; Roldan Cuenya, B., In situ/operando electrocatalyst characterization by X-ray absorption spectroscopy. *Chemical Reviews* **2020,** *121* (2), 882-961.

27. Li, X.; Wang, S.; Li, L.; Sun, Y.; Xie, Y., Progress and perspective for in situ studies of CO_2 reduction. *Journal of the American Chemical Society* **2020,** *142* (21), 9567-9581.

28. Zhu, J.; Wang, P.; Zhang, X.; Zhang, G.; Li, R.; Li, W.; Senftle, T. P.; Liu, W.; Wang, J.; Wang, Y.; Zhang, A.; Fu, Q.; Song, C.; Guo, X., Dynamic structural evolution of iron catalysts involving competitive oxidation and carburization during CO_2 hydrogenation. *Science Advances* **2022,** *8* (5), eabm3629.

29. Klencsar, Z., Mössbauer spectrum analysis by evolution algorithm. *Nuclear Instruments and Methods in Physics Research Section B: Beam Interactions with Materials and Atoms* **1997,** *129* (4), 527-533.

30. Wezendonk, T. A.; Santos, V. P.; Nasalevich, M. A.; Warringa, Q. S.; Dugulan, A. I.; Chojecki, A.; Koeken, A. C.; Ruitenbeek, M.; Meima, G.; Islam, H.-U., Elucidating the nature of Fe species during pyrolysis of the Fe-BTC MOF into highly active and stable Fischer–Tropsch catalysts. *ACS Catalysis* **2016,** *6* (5), 3236-3247.

31. Clark, A. H.; Imbao, J.; Frahm, R.; Nachtegaal, M., ProQEXAFS: a highly optimized parallelized rapid processing software for QEXAFS data. *Journal of Synchrotron Radiation* **2020,** *27* (2), 551-557.

32. Yang, Q.; Kondratenko, V. A.; Petrov, S. A.; Doronkin, D. E.; Saraci, E.; Lund, H.; Arinchtein, A.; Kraehnert, R.; Skrypnik, A. S.; Matvienko, A. A.; Kondratenko, E. V., Identifying Performance Descriptors in CO_2 Hydrogenation over Iron-Based Catalysts Promoted with Alkali Metals. *Angewandte Chemie International Edition* **2022,** *61* (22), e202116517.

33. Zhang, H.; Shen, J.; Ge, X., The reduction behavior of Fe-Mo-O catalysts studied by temperature-programmed reduction combined with in situ Mössbauer spectroscopy and X-ray diffraction. *Journal of Solid State Chemistry* **1995,** *117* (1), 127-135.

34. Puga, A. V., On the nature of active phases and sites in CO and CO_2 hydrogenation catalysts. *Catalysis Science & Technology* **2018,** *8* (22), 5681-5707.

35. Herranz, T.; Rojas, S.; Pérez-Alonso, F. J.; Ojeda, M.; Terreros, P.; Fierro, J. L. G., Genesis of iron carbides and their role in the synthesis of hydrocarbons from synthesis gas. *Journal of catalysis* **2006,** *243* (1), 199-211.

36. Bearden, J. A.; Burr, A., Reevaluation of X-ray atomic energy levels. *Reviews of Modern Physics* **1967,** *39* (1), 125.

37. Gaur, A.; Stehle, M.; Raun, K. V.; Thrane, J.; Jensen, A. D.; Grunwaldt, J. D.; Hoj, M., Structural dynamics of an iron molybdate catalyst under redox cycling conditions studied with in situ multi edge XAS and XRD. *Physical Chemistry Chemical Physics* **2020,** *22* (20), 11713-11723.